

Computational design and experimental testing of a flexible bi-stable airfoil for passive flow control

Anurag Bhattacharyya*, Mark Bashqawi†, Se Yeon Kim‡, Wanzheng Zheng §, Theresa Saxton-Fox ¶, and Kai James ||
University of Illinois at Urbana-Champaign, Urbana, IL, 61801

This study focuses on the design of a novel airfoil camber morphing mechanism using topology optimization that aims to harness the flow field around the airfoil for its actuation. The morphing mechanism is designed using snap-through instabilities for actuation and shape change. The aerodynamic forces on the outer mold line are predicted using a panel method for inviscid effects and Thwaites method for the boundary layer. The results of the computational morphing airfoil design and the predicted aerodynamics are presented. A 3D printed model of the airfoil is tested in a wind tunnel to analyse its camber morphing characteristics.

I. Nomenclature

B	=	FF^T
C	=	Cauchy-Green deformation tensor
C_l	=	section lift coefficient
c	=	chord
E_e	=	effective material stiffness
E_o	=	bulk material stiffness
F	=	deformation gradient
F_{ext}	=	external forces acting on the structure
F_{int}	=	internal forces acting on the structure
J	=	determinant of the deformation gradient
K_{tan}	=	tangent stiffness matrix
L	=	Column vector associated with adjoint sensitivity analysis
L'	=	lift per unit span
l	=	flat plate length
p	=	penalization constant
R	=	Structural force residual
S	=	Second Piola-Kirchoff stress
U_f	=	displacement vector corresponding to degrees of freedom of structure
u_∞	=	freestream velocity
α	=	airfoil angle of attack

II. Introduction

THE term ‘morphing’, from the perspective of aircraft design, refers to any sub-system/parts of an aircraft that are capable of undergoing substantial change in their external shape such that the aircraft performance is significantly altered to better adapt to the changing mission objectives [1]. This has given rise to a growing interest in morphing airfoils whose geometry can be changed throughout use to modify their geometric properties such as thickness and camber. The changing of the airfoil camber could be used to maximize the airfoil’s efficiency for the current flight

*Graduate Research Assistant, Department of Aerospace Engineering, 104 S Wright St, and AIAA Member Grade.

†Undergraduate Research Assistant, Department of Aerospace Engineering, 104 S Wright St, and AIAA Member Grade (if any).

‡Undergraduate Research Assistant, Department of Aerospace Engineering, 104 S Wright St, and AIAA Member Grade (if any).

§Undergraduate Research Assistant, Department of Aerospace Engineering, 104 S Wright St, and AIAA Member Grade (if any).

¶Assistant Professor, Department of Aerospace Engineering, 104 S Wright St, Member AIAA.

||Assistant Professor, Department of Aerospace Engineering, 104 S Wright St, AIAA Member Grade.

condition, as explained in a study of morphing on a NACA 0012 [2]. The airfoil for low lift coefficients was found to perform nearly the same as the morphing airfoil, but at high lift coefficients, the morphing airfoil outperformed the fixed airfoil. The authors also found that there is an optimal morphing angle for a given angle of attack.

Actuated airfoil morphing allows for in-flight changing of a wing cross-section, but comes at the cost of energy needed for the actuation. An investigation into minimizing drag and energy use was done by Namgoong et al. [3]. The authors found that the energy could be modelled by the strain energy of the deformed structure and the effect of aerodynamic forces from deformation. The model was developed with respect to minimizing the drag during various flight conditions to implement a multi-objective design. Morphing airfoils can also act as control surfaces and flaps while still remaining as a single element. A numerical and wind tunnel investigation was made that compared a hinged flap to a trailing edge morphing airfoil [4]. The morphing airfoil was found to exhibit better lift coefficient properties than the flapped airfoil at equivalent angles of attack and flap deflection [4].

Actuated morphing during flight could also reduce the effects of stall by reducing the top curvature of the airfoil [5], but the required actuation energy, weight, and complexity reduce the overall efficiency of the design. Several authors have investigated different mechanization and actuation techniques to design morphing structures with improved aerodynamic properties. A biologically inspired morphing concept, FishBAC, was proposed by Woods et al. [6]. It included an antagonistic pair of tendons and a non-backdriveable spooling pulley integrated with a flexible skeletal core for deflections. The drag produced by the concept was observed to be lower than that of a NACA 0012 airfoil with a discrete trailing edge flap. Bi-stable structural solutions, due to their inherent ability to deform and maintain equilibrium, have also been widely explored for potential morphing applications. Diaconu et al. [7] used non-symmetric laminate configurations of carbon-fiber laminated composites and induced residual stresses to design camber and chord morphing structures. Pontecorvo et al. [8] investigated the use of bi-stable arches, made of NiTiNOL and Delrin, for morphing applications. Their study focused on the influence of different structural parameters in the design of a bistable arch to meet morphing requirements. A passive system that responds based on aerodynamic forces removes the need for heavy actuators. This paper looks to investigate how an airfoil can be designed to passively morph to prevent or respond to stall.

Keeping in mind the benefits that can be derived from the implementation of passively morphing structures, the use of compliant mechanisms for changing the shape of leading and trailing sections of an airfoil using a single actuator force has been investigated by Saggere and Kota [9]. Smart and active materials like shape memory polymers (SMP) and shape memory alloys (SMA) have also been investigated for designing morphing airfoil structures[10–13]. The current study uses snap-through instability to design a bi-stable mechanism for an airfoil that uses the pressure field around it for actuation into multiple stable configurations. In the computational design domain, topology optimization has been used widely to design materials and structures with unique multi-physics properties. A comprehensive list of articles highlighting studies on computational design with topology optimization and focusing on bi-stable structural design along with the design methodology for bi-stable camber morphing airfoil can be found in [14].

To design a practical camber morphing airfoil, it is required to integrate the aerodynamic forces on the OML with the internal structural design methodology. Methods for estimating the aerodynamics around the airfoil include computational fluid dynamics (CFD), such as OpenFOAM and Ansys-Fluent, and panel methods, such as XFOil. Dhileep et al. [2] compared the CFD solvers to the panel solver to determine the viability of the XFOil solver given its lower computational cost. The XFOil predictions were found to result in lower drag values than the CFD solvers but were still accurate in the computed pressure coefficient. Nordin [15] used a modified panel method to predict the inviscid and viscous aerodynamic effects. The method employed a source and vortex potential flow panel method for the inviscid effects. Various boundary layer methods were examined for predicting laminar and turbulent boundary layer effects which were coupled with the panel method for a complete force distribution. For the laminar boundary layer, Thwaites method was found to present more accurate results for thicker airfoils than the other methods. For turbulent boundary layers, Head's method was chosen for its simplicity [15].

To predict the aerodynamics of the airfoil presented in this paper, a panel method code with boundary layer estimations was implemented to quickly determine the forces on the whole airfoil and on the force-sensitive morphing components. To validate and test the computational estimation of the morphing airfoil's behavior, an experiment was designed for implementation in a wind tunnel. The morphing airfoil was 3-D printed and connected to two load cells to measure overall lift and drag [16]. The assembly will be vertically mounted in a wind tunnel, and measurements will be performed to verify the force at which the airfoil morphs [17]. The final paper will show the results of the experiment and compare them with the computational predictions.

This paper is organized as follows: The overall design philosophy is discussed in section III. The structural design of the morphing airfoil is presented in Sections IV A. The aerodynamics prediction methodology is explained in more

detail in Section IV B. The methods of communication between the structural design and aerodynamic prediction are presented in Section IV C. Section V focuses on the design of the experimental setup. The results of the structural and aerodynamic design methods are presented in Section VI.

III. Design Overview

The main idea is to design a camber morphing airfoil, actuated by harnessing the pressure field on the Outer Mold Line (OML). During high-lift maneuvers, the airfoil will assume a high-camber configuration. This position is termed as the *activated* airfoil configuration. This *activated* configuration corresponds to the deformed state, one of the two stable states of a bi-stable structural system. If the angle of attack increases while in the activated state, this will cause an increase in the aerodynamic forces at the trailing edge of the lower surface of the airfoil. This change in loading will naturally trigger a snap-through response in which the airfoil transitions to a low-camber shape (i.e. an *inactive* state), thereby preventing flow separation. This *inactive* state is the second stable state of the bi-stable structural system. Thus, the proposed design methodology integrates bi-stable mechanism design methods to design a camber morphing airfoil using aerodynamic pressure on the trailing edge surfaces for actuation. The design philosophy has been schematically represented in Figure 1.

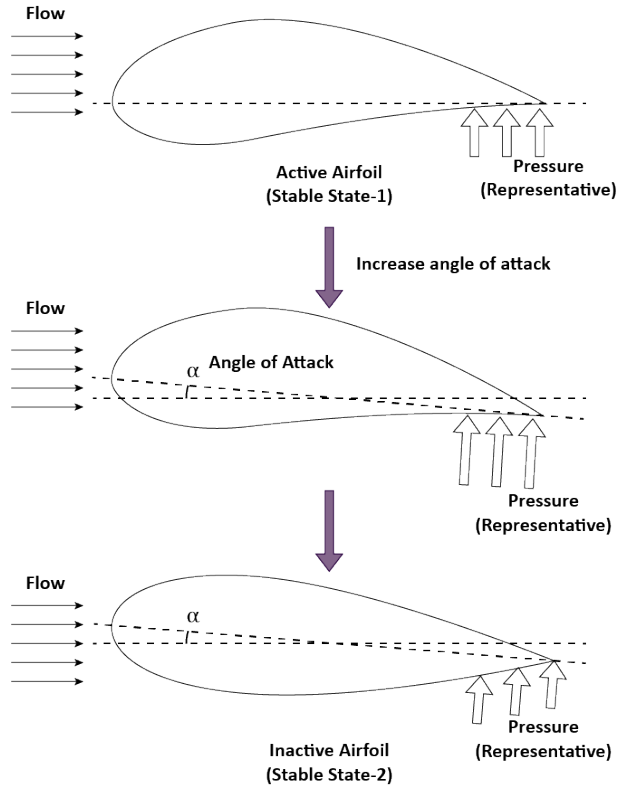


Fig. 1 Design Philosophy: Bi-stable camber morphing airfoil design actuated through aerodynamic forces.

IV. Computational methods

A. Structural design using topology optimization

In topology optimization, a given amount of material is optimally distributed within a design domain subjected to certain loading and boundary conditions such that a given cost/objective function is minimized. The optimal material distribution is determined by carrying out the finite element analysis in combination with a SIMP (*solid isotropic material penalization*) scheme for material parameter interpolation. The effective material properties for each element

are evaluated as:

$$\Psi_{eff} = \Psi_1 + \rho^p (\Psi_2 - \Psi_1) \quad (1)$$

Here, Ψ represents a generic material parameter, ρ is the mixing ratio which ranges from 0 to 1 and p represents the penalization constant. Generally, p is chosen to be a number greater than 1 to ensure that the intermediate densities are penalized and removed from the optimal design. The effective stiffness of each element, E_e , for a void-solid material combination is represented as

$$E_e = \rho^p E_0 \quad (2)$$

where $\rho \in [0,1]$ is the volume fraction for each element. E_0 is the bulk material stiffness of the solid and p is the SIMP penalization parameter. In standard linear elastic problems selecting $\rho_{min} > 0$ prevents the global stiffness matrix from becoming singular. At smaller values of ρ_{min} , the finite element evaluation diverges due to severe mesh distortions and the emergence of degenerate elements. The design of bi-stable mechanisms involves relatively large displacements, and because we are modeling geometric nonlinearity of structures, the algorithm is susceptible to divergence. This forces us to use a higher value of ρ_{min} to stabilize the algorithm.

To get rid of numerical instabilities [18][19] that give rise to mesh-dependent designs and appearance of checkerboard patterns due to the use of lower-order finite elements and a discrete density distribution, a density filtering technique introduced by Bruns and Tortorelli [20] is implemented.

1. Bi-Stable Airfoil Design

The key design aspects of a bi-stable beam [14] are incorporated into the design of a bi-stable airfoil. The airfoil design domain along with the finite element mesh is shown in Figure. 2. The finite element mesh is generated using ABAQUS software. For the computational design study, an airfoil with chord length of 100 mm and maximum thickness of 30 mm is chosen. The functional aspects of the wing spars are simulated by fixing certain nodes inside the airfoil domain shown by the ‘black’ markers. These constitute the fixed boundaries of the design domain for the finite element analysis. The airfoil design domain is discretized with an unstructured mesh consisting of 1925 triangular finite elements.

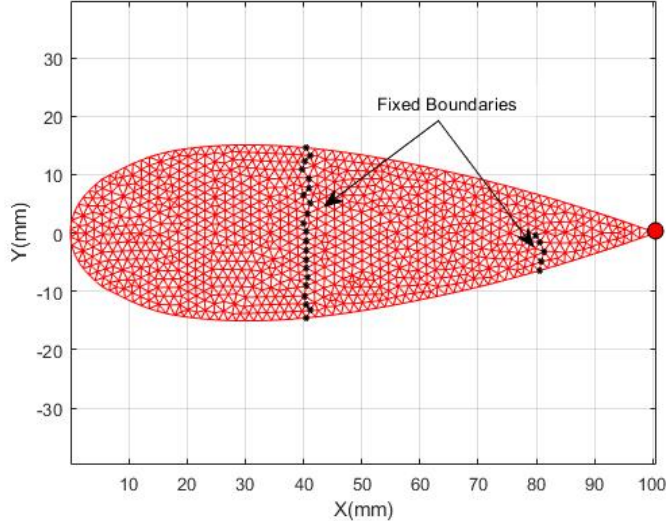


Fig. 2 Design domain for the morphing airfoil optimization problem

The goal is to generate a mechanism, using topology optimization, inside the design domain capable of deflecting the trailing edge into two stable configurations using the aerodynamic forces generated due to the fluid flow around it. The trailing edge deflections are measured by the displacement of the node shown by the ‘red’ marker on the trailing edge. Here, a displacement controlled method for structural analysis is used. In this method, the actuating node (‘red’ node) is displaced successively to values u_1 and u_2 . The corresponding forces required are represented as θ_1 and θ_2 as shown in the Figure 3. For this analysis, u_1 and u_2 are chosen as 2 mm and 7 mm, respectively. This represents the

force-displacement curve corresponding to the baseline (un-optimised) domain. Topology optimization is used to tailor the path of this force-displacement curve so that the applied force θ_2 , at displacement state u_2 , is negative. The resulting bimodal curve will correspond to a bi-stable structural design [14].

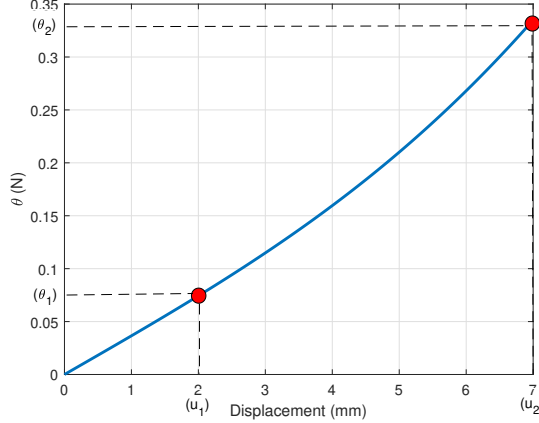


Fig. 3 Force-displacement curve the baseline (un-optimized) design domain.

Therefore, the objective of the optimization problem is to minimize force (θ_2) required to deflect the trailing node. To ensure proper structural rigidity at the bi-stable region, we constrain the force (θ_1) corresponding to the first displacement (u_1) to be of value greater than, F_{min} . The value of F_{min} is chosen to be 20% of the force corresponding to u_1 for the solid baseline design domain. The volume constraint $V(\rho)$ controls what percent of the original design domain will form the optimized structure. Apart from these, the reaction forces along the x -axis, at the fixed boundaries, were also constrained to be greater than certain limiting values. Mathematically we can represent these as follows

$$\begin{aligned} & \underset{\rho}{\text{minimize}} \quad \theta_2 \\ & \text{subject to} \quad \theta_1 \geq F_{min}, \\ & \quad V(\rho) \leq V_0 \\ & \quad \mathbf{R}_{L_x} \leq R_{L_o} \\ & \quad \mathbf{R}_{R_x} \leq R_{R_o} \end{aligned} \tag{3}$$

Here \mathbf{R}_{L_x} and \mathbf{R}_{R_x} are the sum of reaction forces on the nodes along the x -axis on the left and right fixed boundary surfaces respectively. The parameters R_{L_o} and R_{R_o} are the maximum values of reaction forces allowed on the left and the right fixed boundaries respectively. They are chosen to be equal to 90% of the sum of the nodal reaction force values along the x -axis for each of the fixed boundaries for the baseline (un-optimised) configuration.

2. Large Deformation Modeling

In this study, the large deformations undergone by the morphing structure are modelled using the neo-Hookean material model [21][22][23]. The potential energy function for the material is defined as:

$$\Phi = \frac{1}{2}\lambda_0[\ln J]^2 - \mu_0 \ln J + \frac{1}{2}\mu_0[\text{tr}(\mathbf{C}) - 3] \tag{4}$$

where λ_0 and μ_0 are the Lamé constants. The term J is the determinant of the deformation gradient, \mathbf{F} . The term $\text{tr}(\mathbf{C})$ denotes the trace of the right Cauchy-Green deformation tensor ((\mathbf{C})). The Second Piola-Kirchoff stress, \mathbf{S} , can be calculated as:

$$\mathbf{S} = 2 \frac{\partial \Phi}{\partial \mathbf{C}} = \lambda_0[\ln J]\mathbf{C}^{-1} + \mu_0(\mathbf{I} - \mathbf{C}^{-1}) \tag{5}$$

Here \mathbf{I} is the Identity tensor. The Cauchy stress, $\boldsymbol{\sigma}$, is defined as

$$\boldsymbol{\sigma} = \frac{1}{J} \mathbf{F} \mathbf{S} \mathbf{F}^T = \frac{1}{J} [\lambda_0 [\ln J] \mathbf{I} + \mu_0 (\mathbf{B} - \mathbf{I})] \quad (6)$$

where $\mathbf{B} = \mathbf{F} \mathbf{F}^T$. The structural equilibrium equation can be written as:

$$\mathbf{R} = \mathbf{F}_{ext} - \mathbf{F}_{int} = \mathbf{0} \quad (7)$$

where \mathbf{F}_{ext} and \mathbf{F}_{int} are the external and the internal forces acting on the structure. The equation 7 is a nonlinear equation and is solved iteratively using a Newton-Raphson procedure as outlined by Dhatt & Batoz [24]. The incremental displacements ($\Delta \mathbf{U}$) are updated using

$$\mathbf{K}_{tan} \Delta \mathbf{U} = \mathbf{R} \quad (8)$$

here \mathbf{K}_{tan} is called the tangent stiffness matrix. Here we use a displacement controlled method is used to solve the governing equation, $\mathbf{R} = 0$. The external force, \mathbf{F}_{ext} is defined as:

$$\mathbf{F}_{ext} = \theta \mathbf{F}_0 \quad (9)$$

where \mathbf{F}_0 is a sparse reference vector of size equal to the number of degrees of freedom and a unit value at the degree of freedom corresponding to the prescribed displacement.

3. Adjoint Sensitivity Analysis

Sensitivity analysis is performed to compute the gradient of the objective function and is passed to the optimization algorithm. The gradient values are computed using the adjoint sensitivity analysis procedure [25]. Let the objective function be defined as

$$\Pi = \Theta(\mathbf{U}_f(\boldsymbol{\rho}), \boldsymbol{\rho}) \quad (10)$$

Where Θ be the response objective function, \mathbf{U}_f defines the displacement vector corresponding to the free degrees of freedom of the structure and $\boldsymbol{\rho}$ is the vector of design variables. The structure to be in equilibrium has to satisfy the condition that the residual, \mathbf{R} , should be equal to zero for each deformed configuration.

$$\mathbf{R}(\mathbf{U}_f(\boldsymbol{\rho}), \boldsymbol{\rho}) = \mathbf{0} \quad (11)$$

The objective function is combined with the equilibrium constraint to form the augmented Lagrangian function, L , as:

$$L = \Theta + \lambda^T \mathbf{R} \quad (12)$$

where λ is a Lagrange multiplier. It can be observed that L is identically equal to the objective function, Θ , for all λ , since \mathbf{R} is zero, as shown in equation 11. Hence, the sensitivity of L with respect to the design variable, $\boldsymbol{\rho}$, is the same as the sensitivity of the response function, Θ . Using the chain rule of differentiation, we can write

$$\frac{dL}{d\boldsymbol{\rho}} = \frac{\partial \Theta}{\partial \boldsymbol{\rho}} + \frac{\partial \Theta}{\partial \mathbf{U}_f} \frac{d\mathbf{U}_f}{d\boldsymbol{\rho}} + \lambda^T \left[\frac{\partial \mathbf{R}}{\partial \mathbf{U}_f} \frac{d\mathbf{U}_f}{d\boldsymbol{\rho}} + \frac{\partial \mathbf{R}}{\partial \boldsymbol{\rho}} \right] \quad (13)$$

The operator $\frac{\partial}{\partial \boldsymbol{\rho}}$ captures the explicit dependence of the function applied to with respect to $\boldsymbol{\rho}$. Whereas, the operator $\frac{d}{d\boldsymbol{\rho}}$ captures the indirect dependence of a function with respect to variable $\boldsymbol{\rho}$. Collecting the implicit derivatives and grouping them together, we get

$$\frac{dL}{d\boldsymbol{\rho}} = \frac{\partial \Theta}{\partial \boldsymbol{\rho}} + \lambda^T \frac{\partial \mathbf{R}}{\partial \boldsymbol{\rho}} + \left[\lambda^T \frac{\partial \mathbf{R}}{\partial \mathbf{U}_f} + \frac{\partial \Theta}{\partial \mathbf{U}_f} \right] \frac{d\mathbf{U}_f}{d\boldsymbol{\rho}} \quad (14)$$

Since λ^T is arbitrary, it is selected such that the coefficients of the the implicit terms vanish. Thus the value of λ^T can be written as:

$$\lambda^T = - \left[\frac{\partial \mathbf{R}}{\partial \mathbf{U}_f} \right]^{-T} \frac{\partial \Theta}{\partial \mathbf{U}_f}^T = - \mathbf{K}_{tan}^{-T} \frac{\partial \Theta}{\partial \mathbf{U}_f}^T \quad (15)$$

Here, λ is called the adjoint response and \mathbf{K}_{tan} is the tangent stiffness matrix. After obtaining the adjoint response, it is substituted in equation 14, to get the total derivative as:

$$\frac{dL}{d\rho} = \frac{\partial\Theta}{\partial\rho} + \lambda^T \frac{\partial\mathbf{R}}{\partial\rho} \quad (16)$$

The optimization algorithm chosen for solving the structural optimization problem is the Method of Moving Asymptotes (MMA) [26]. Within each optimization iteration, the optimizer solves a convex approximation of the nonlinear programming problem. The optimizer terminates when the first order Karush-Kuhn-Tucker (KKT) conditions are satisfied [27][28].

B. Aerodynamic force prediction

The aerodynamic inviscid and viscous forces on the airfoil were predicted computationally. The computational methods were capable of isolating forces along particular regions of the airfoil, such as along the passively morphing portion, and integrating those forces to compute an overall force prediction. These methods included a vortex-source panel method for the inviscid prediction with Thwaites and Blasius methods for the viscous boundary layer. Head's method for turbulent boundary layers will be used for the final paper instead of Blasius.

To provide an inviscid prediction of the flow field around the geometry, potential flow theory was used to develop a panel method. This theory assumes an incompressible, inviscid, and irrotational fluid and provides a reasonable estimate for low Mach number flows. Flow tangency and the Kutta condition were also enforced to allow for a realistic and simple solution.

To implement, the geometry was represented by a series of n flat panels. Each panel had a uniform source sheet, which pushed the flow away from the panels, and a uniform vortex sheet, which provided circulation effects due to the airfoil curvature [15]. To enforce flow tangency, the total normal velocity at each panel's center due to the combined effects of the source, vortices, and freestream was set to zero. This resulted in a set of n equations and n source strengths to solve for. The vortex strength across the geometry was equal for every panel, so only one vortex strength needed to be solved for, adding one more variable. To obtain the last equation for this variable, the Kutta condition was set by requiring the tangential velocities of the trailing edge panels to be equal. Overall, there were $n+1$ equations and $n+1$ variables that could be solved as a linear system for the source and vortex strengths. With all the strengths known, the flow velocity field could be found.

To obtain more accurate results, a boundary layer estimation was used for viscous effects as a supplement to the inviscid panel method solution. For a laminar boundary layer, Thwaites method was used, which is built on Pohlhausen's boundary layer approximation combined with empirical data as described by Thwaites [29]. The empirical approximations allowed for quick calculations of the momentum thickness, displacement thickness, and local skin friction coefficient. The laminar separation point could then be found where the skin friction coefficient was zero.

For the current code, Thwaites method was used until separation where the Blasius solution was used to estimate the boundary layer properties for the remaining length of the airfoil. The Blasius equations are exact solutions to the boundary layer equations for zero pressure gradient flows along a flat plate and are described by Blasius in [30].

The boundary layer and inviscid methods were coupled and the combined system was iterated upon until convergence. The boundary layer method required knowledge of the local flow velocity from the inviscid method, and the boundary layer's displacement thickness acted as a modified body edge about which to compute the inviscid flow. The computation of the inviscid and viscous flows were repeated until the displacement thickness converged to a fixed value.

Once the inviscid flow and boundary layers were estimated, the pressure and skin friction coefficients could be calculated. These coefficients were used to obtain the forces and moments on each panel, giving a force distribution across the entire airfoil. Summing these forces and moments over a set of specified panels gave the force acting on a specific region of the airfoil. This was used to predict the force on the trailing edge flap of the morphing airfoil.

1. Validation

To verify the implemented inviscid panel method alone, the lift coefficient for a NACA 0012 airfoil calculated using the panel method code was plotted versus angle of attack, α . This lift coefficient was defined as

$$C_l = \frac{L'}{\frac{1}{2}\rho_\infty u_\infty^2 c} \quad (17)$$

where L' is the lift per unit span, ρ_∞ is the air density, u_∞ is the wind speed, and c is the airfoil chord. Data from a wind tunnel test [31] was plotted in comparison to the computational predictions. Fig. 4 shows that the panel method lift prediction predicts the correct values up to about eight degrees of angle of attack, where viscous effects begin to have a noticeable impact. This matches the expected behavior for the inviscid panel method.

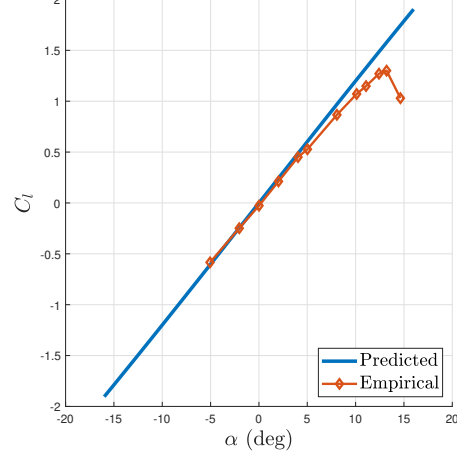


Fig. 4 Lift curve predicted by panel method code plotted with wind tunnel data [31].

The lift, drag, and moment coefficients for a NACA 0012 were also plotted against the number of panels used at an angle of attack of 6 degrees, shown in Fig. 5. Since the panel method is inviscid, the drag should approach zero as the number of panels increases, which is seen in the figure. The lift and moment also converge as the number of panels increases. Figure 5 suggests that 200 panels is sufficient for a good inviscid flow estimation.

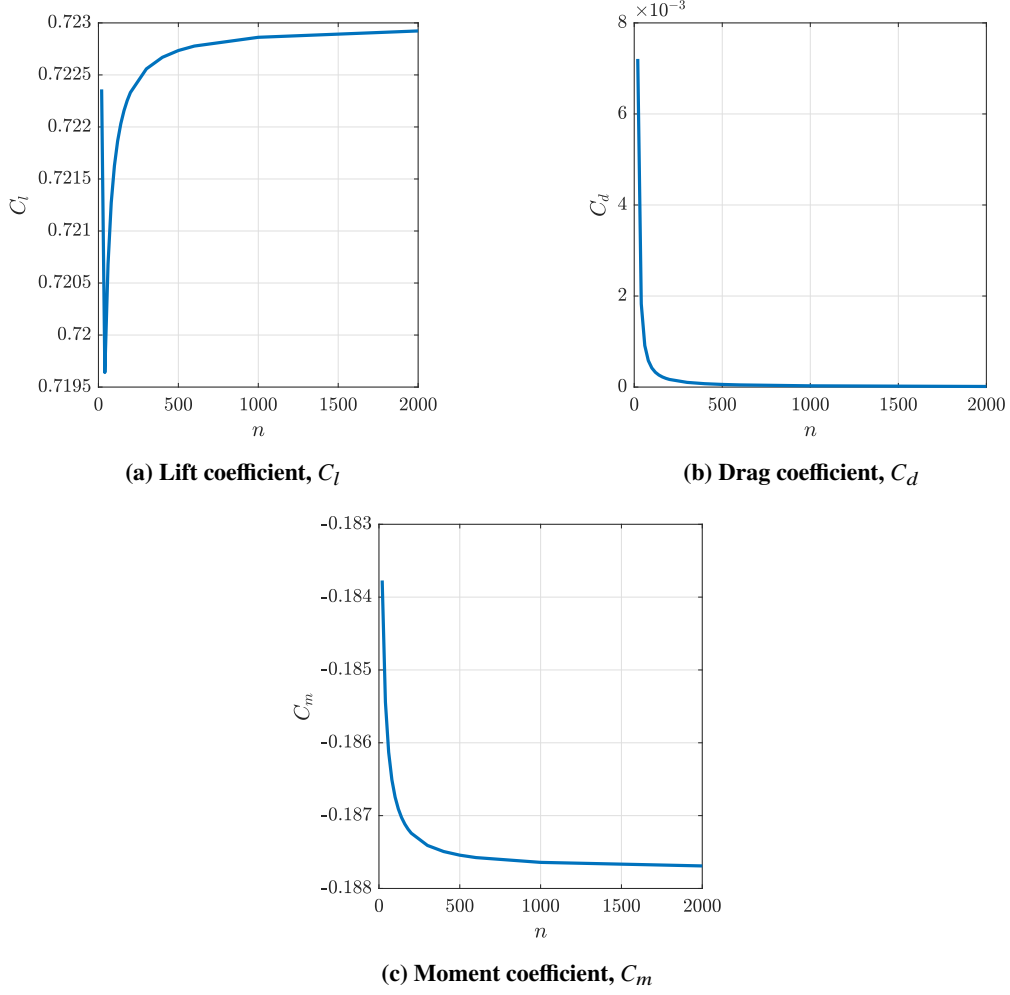


Fig. 5 Lift, drag, and moment coefficients at 6 degrees angle of attack versus number of panels.

To verify the implementation of Thwaites method, the code was run for a zero-pressure gradient flat plate as this flow has simple exact solutions to compare to. For the flat plate, the Blasius boundary layer solutions were used to compare with the Thwaites solution, shown in Fig. 6 where l is the length of the plate used to normalize the axes. The maximum error for the calculated displacement thickness between the Thwaites and Blasius methods was less than half a percent.

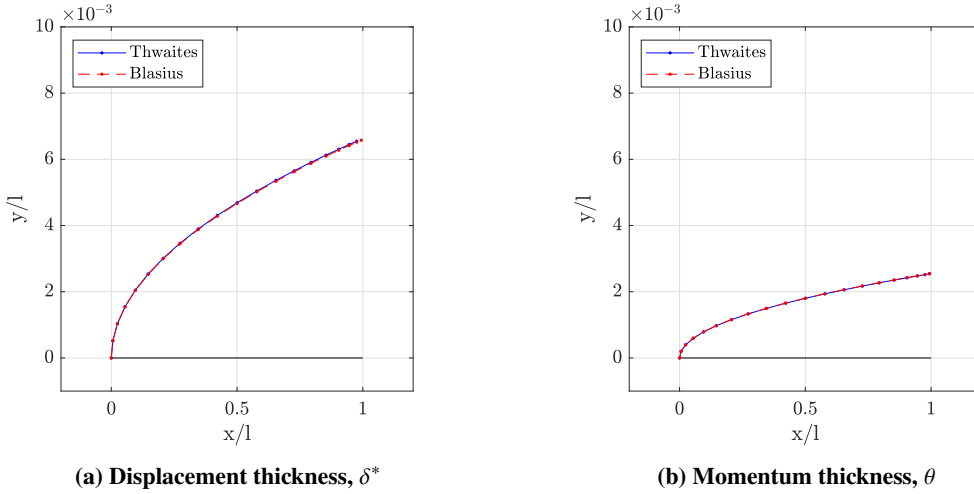


Fig. 6 Boundary layer heights predicted by Blasius solutions and implemented Thwaites method.

C. Communication between methods

The structural design and aerodynamic force predictions are coupled: the shape of the design affects the aerodynamic forces, and the aerodynamic forces affect the structural deflection, therefore the structural design must account for this coupling. To connect the two computational frameworks, an initial material distribution was generated with a nominal force acting on the trailing edge node as shown by the ‘red’ marker in Figure 2. After the initial design, aerodynamic forces on the trailing edge were predicted. These forces were used to modify the camber morphing airfoil and characterise its morphing behavior. The idea of using the morphed cambered stable state as the baseline configuration was explored and the angle of attack at which this configuration reverted back to the un-cambered position was investigated.

D. Validation: A One-way Fluid Structure Interaction (FSI) Analysis

A one-way fluid-structure interaction (FSI) analysis is set up in Ansys to determine the aerodynamic characteristics of the initial structural design of the morphing airfoil. The work flow can be defined as follows:

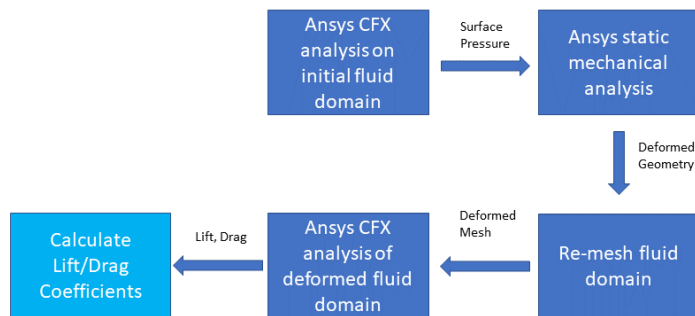


Fig. 7 Flowchart of the FSI analysis

The initial result states that snap-through occurs at 50 degrees angle of attack in flow of 25m/s and 30 degrees angle of attack in flow of 80m/s. However, these locations are well past stall for the adopted airfoil. The Lift versus angle of attack graph is shown as in Figure 8. While the critical angle-of-attack at which the airfoil transitions from a low-camber shape to a high-camber shape is significantly higher than the desired snap-through point, this result is somewhat promising. Figure 8 shows that with a single airfoil, and without the need for complex actuators, we are able to drastically shift the airfoil’s aerodynamic properties in response to changing flight conditions. As desired, at low

angles of attack, the flexible airfoil behaves similar to the rigid high-camber airfoil, and at high angles of attack, the flexible airfoil behaves similar to the rigid no-camber airfoil.

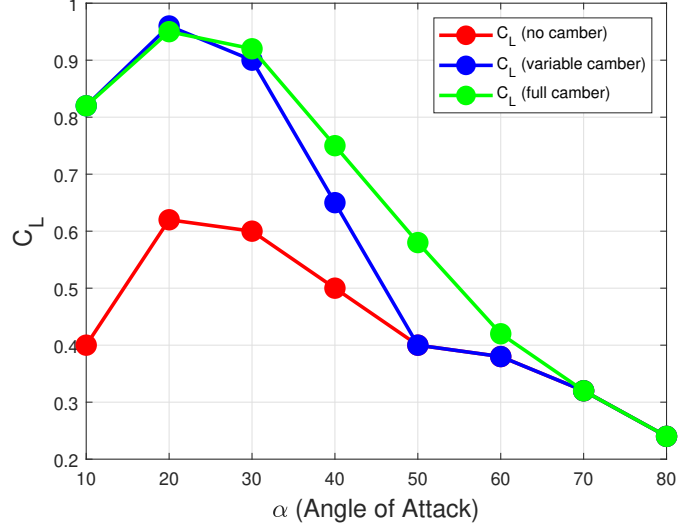


Fig. 8 C_L vs α based on one-way Ansys FSI analysis

V. Experimental methods

A. 3D Printing

An airfoil CAD design was derived from topology optimization result by tracing the black outer mold line of the pixelized material domain, shown in Figure 12a. Grey elements in the figure were interpreted as thinner material that served as a hinge connecting the morphing structures, and fixed boundaries were interpreted as pinpoint interfaces between rigid and flexible material. The design was tested in an ANSYS mechanical solver for further validation of bi-stability, and a few trial-and-error runs, specifically for determining the thickness of the hinge, were performed while transferring the topology optimization result into a printable state. The first prototype airfoil had an aspect ratio of 2, with a 3-inch in chord and 6 inch in span, for ease of mounting onto the test stand. Materials used in the printing process were chosen, based on a previous study [32], to be VeroWhite and TangoBlack for the rigid leading edge and deformable trailing edge, respectively. The printed airfoil, shown in Figure 9a-9d will be tested in a wind tunnel for examination of aerodynamic properties.

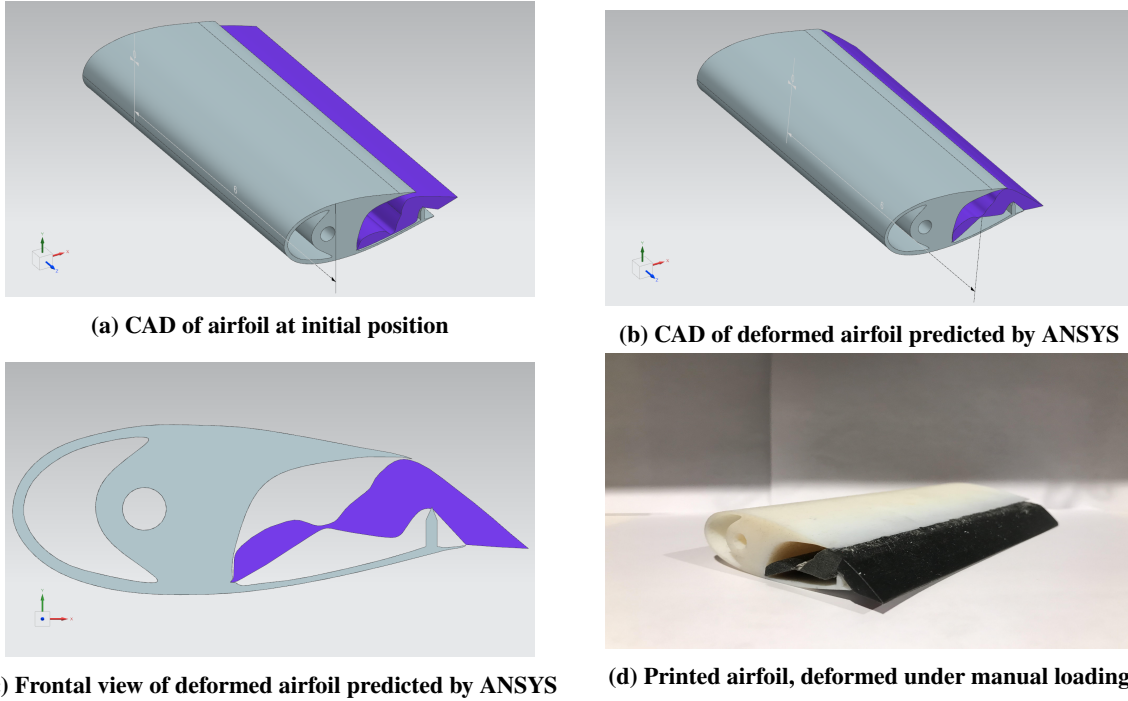


Fig. 9 Design of prototype airfoil

B. Wind tunnel testing of printed prototype

A 3-D printed airfoil is tested in a wind tunnel to measure the forces generated and the force at which the airfoil passively morphs. To directly measure the lift and drag of the morphing airfoil, two load cells in perpendicular positions are utilized. The load cells used were Spark Fun Electronics model TAL220B with a capacity of 5 kgf. The model has the rated output of $1.0 \pm 0.1 mV/V$ and the combined error of $\pm 0.05\% FS$. Figure 10 illustrates the computer-aided design of the device, and Figure 11 shows the implementation of the prototype. The airfoil of span length of 6 in and chord length of 3 in was mounted vertically to neglect the effect of gravity. The rod, which goes through the airfoil along its span, controlled the angle of attack and connected the airfoil to the load cells. A printed part was made from PLA material to hold the assembly together. With the 3-D printed airfoil connected to the test assembly, the load cells for lift and drag measurements are calibrated and measurements are taken at various aerodynamic conditions. The setup of the experiment is located in a $15'' \times 15''$ subsonic wind tunnel at Aerodynamic Research Laboratory at the University of Illinois at Urbana-Champaign.

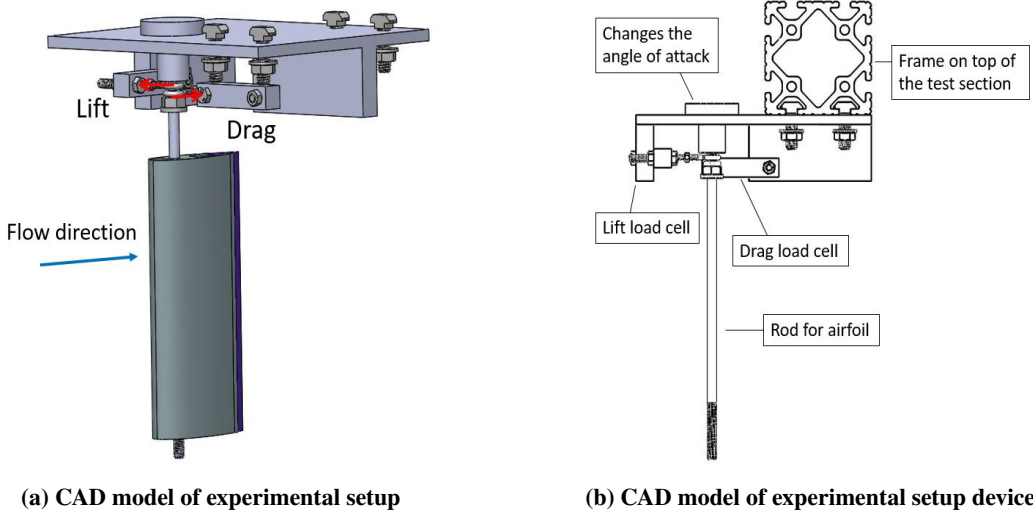


Fig. 10 CAD model of experimental setup of lift and drag measurements

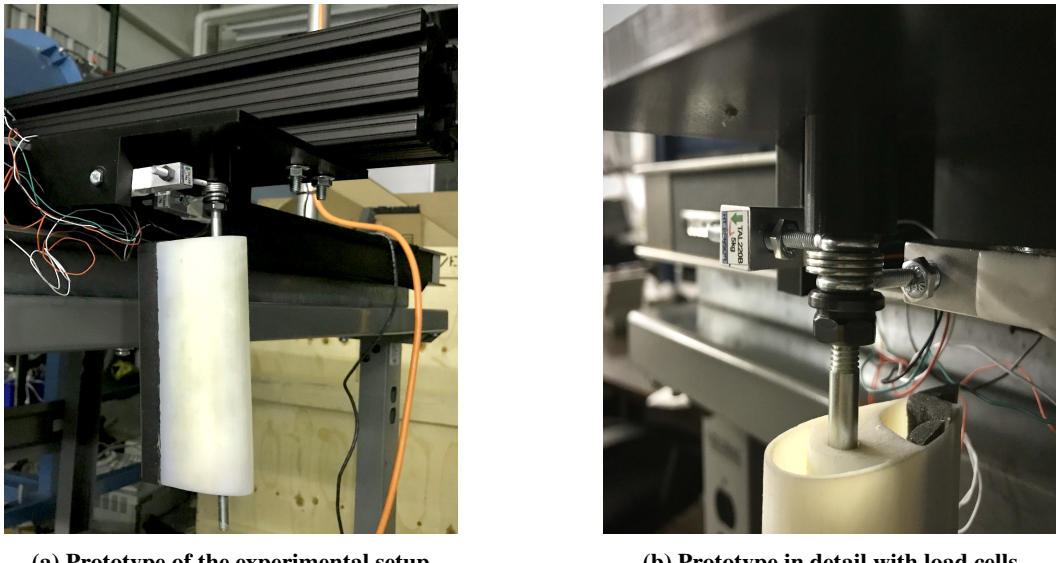


Fig. 11 Prototype of experimental setup of lift and drag measurements

The results of the experiment is compared to those of the computation with matching dimensions of the airfoil, wind tunnel speed, and ambient conditions. The wind tunnel speed is specified at 20 m/s, with a Reynolds number of approximately 1.012×10^5 defined using the chord length of the airfoil. Uncertainty analysis and consideration of errors, such as sensitivity resulting from the vibration of the wind tunnel and possible inaccuracy of the load cells, is carried out for the experimental data. Discrepancies between the computation and the experiment are expected due to three-dimensional effects. To minimize the 3-D effects, the use of end plates and maximizing the aspect ratio within the physical limits of the testing section has been considered.

VI. Results

Figure 12 shows the results obtained from the topology optimization algorithm with the conditions and constraints as outlined in Equation 3. Figure 12a represents the optimized design domain generating the bi-stable mechanism.

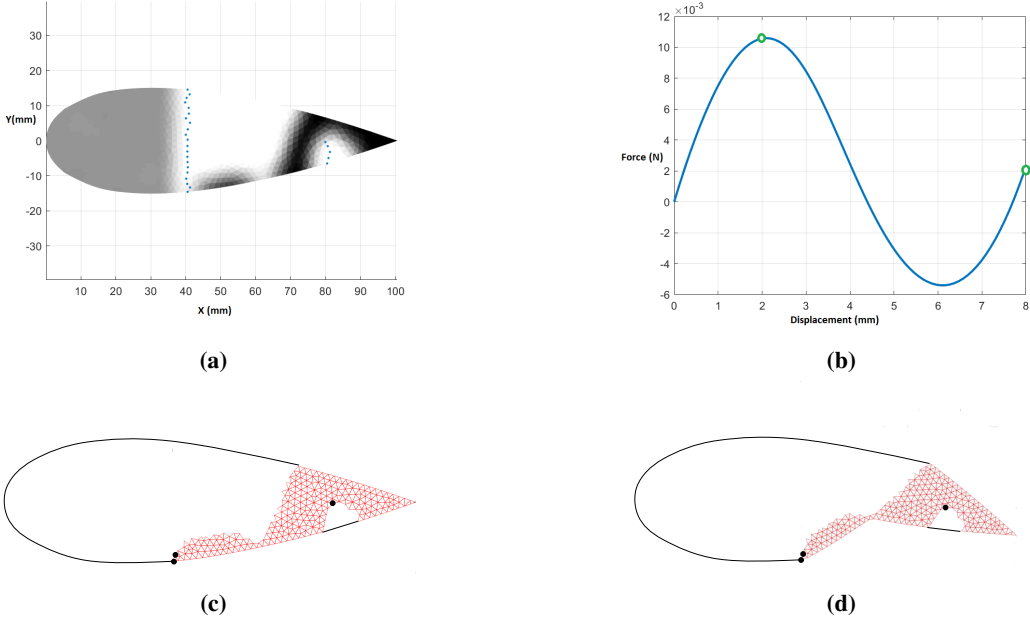


Fig. 12 (a) Optimized material distribution inside the airfoil domain. (b) Force-displacement curve exhibiting bi-modal nature. (c) FEA mesh in undeformed configuration. (d) FEA mesh in deformed configuration.

We observe that there is a significant portion of non-functional (grey) material distributed near the leading edge region of the optimized airfoil. This material is placed by the optimizer to satisfy the volume constraint and is separated from the rest of the airfoil. Hence, this material can be safely removed during post-processing of the generated results. During the post-processing phase the elements corresponding to the void material are also removed. Figure 12b shows the bi-modal nature of the force-displacement curve, validating the bi-stable structural characteristics. After obtaining the optimized material distribution, the forward analysis is carried for this design, with u_1 kept same as 2 mm but u_2 is increased from 7 mm to 8 mm to obtain the full force-displacement characteristics of the bi-stable mechanism. Figures 12c and 12d shows the post-processed mesh in the un-deformed and the deformed configurations.

The aerodynamic force code was run for the airfoil geometry in the high-camber configuration given in Fig. 13a at freestream velocities of 20 m/s, chord lengths of 76 mm, and a span of 152 mm. These parameters were chosen based on the wind tunnel used for testing the printed geometry and constraints of the 3D printer. The forces along the surface of the airfoil at zero angle of attack are shown in figure 13. The forces across most of the top and bottom of the airfoil are equal, which should be true for zero angle of attack. Along the morphed section, the uneven force distribution results in a net force on the morphing member and the rest of the airfoil. The forces on the region simulating the morphing component of the airfoil are shown in Fig. 13b which indicate a net force in the axial and normal directions of the airfoil.

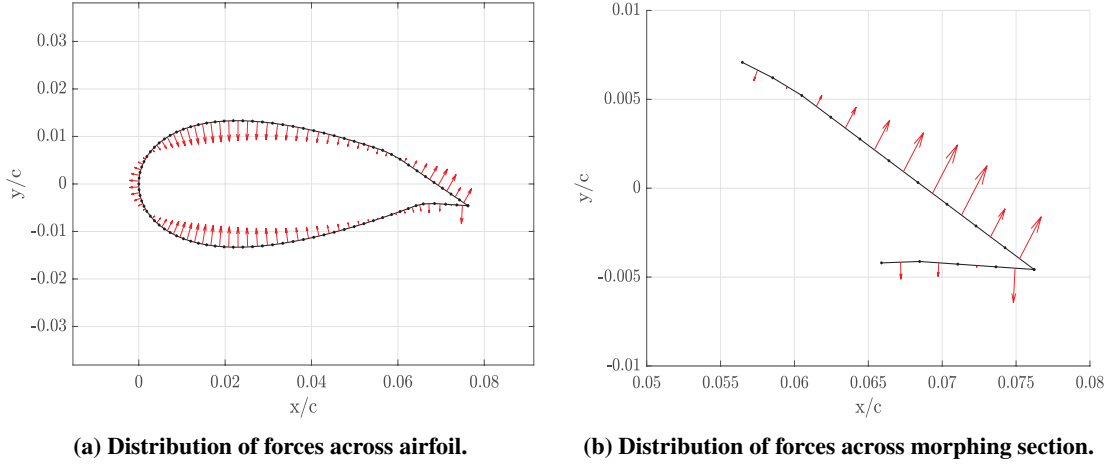


Fig. 13 Distribution of forces at zero degrees angle of attack.

A. Wind Tunnel Experiment

Wind tunnel experiments were performed to test the snap-through capabilities of the initial structural design of the morphing airfoil. The airfoil was mounted in a wind tunnel with a free-stream speed of 20 m/s and its angle of attack was systematically varied between 0 and 65 degrees. The tip deflection of the airfoil was estimated visually at six angles of attack, as shown in Figure 14, and compared to the predictions made using Ansys. The experimental results agreed well with the Ansys predictions, suggesting that the computational framework is ready to be used iteratively to drive the design towards specific aerodynamic control aims.

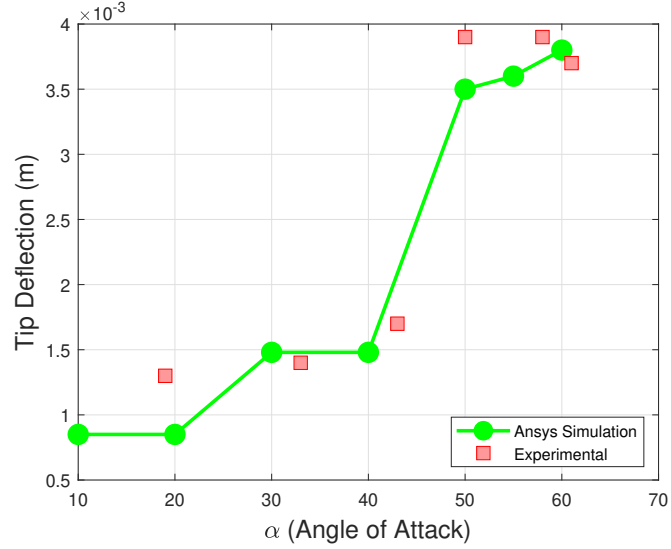


Fig. 14 Comparison of Ansys simulation results with wind tunnel experiment at $25ms^{-1}$

We observe that the experimental result and FEM predictions align well. Preliminary lift and drag data were measured using load cells. Calibration and analysis is on-going, but in future work, lift and drag data will be used to further validate and inform the computational design approach.

VII. Conclusion

A passively morphing airfoil that responds to aerodynamic forces on its OML was designed using a topology optimization framework. The optimization algorithm used nonlinear finite element analysis with a neo-Hookean material model to simulate the large-deformation response of the airfoil mechanism. Appropriate boundary conditions and a corresponding optimization problem formulation were chosen to achieve a desired bi-stable elastic response in which the airfoil can assume two fully stable equilibrium shapes, one high-camber and one low-camber. The transition from the high-camber shape to the low-camber shape has been explored to prevent flow separation. The aerodynamic forces expected to act on the airfoil were predicted using an in-house code that uses a panel method and Thwaites method. A one-way fluid-structure interaction analysis was also carried out using Ansys simulations to quantify the aerodynamic characteristics of the design. A prototype morphing airfoil geometry was printed and tested in a wind tunnel in the high cambered position and the angle of attack at which it snapped back to its stable un-cambered position was measured. The experimentally observed angle of attack matched with the simulation results with satisfactory agreement. We also successfully demonstrated the ability to create a passively morphing airfoil whose aerodynamic characteristics change considerably in flight when exposed to changes in the flow field. Further investigation is required to achieve more precise tailoring of the airfoil's snap-through point. In particular, future research should focus on achieving an airfoil whose limit point is calibrated so that the airfoil transitions prior to flow separation, in order to prevent stall and the sudden loss of lift. Future work will investigate the use of a modified topology optimization method in which the locations of the structural supports are optimized simultaneously with the internal material distribution. Additionally we will investigate the use of a coupled aeroelastic model in which the forces acting on the structure during the topology optimization are obtained directly from an aerodynamic analysis. Ultimately, the ability to achieve targeted, passive morphing without the need for complex, heavy actuator systems, can lead to lighter, more reliable aircraft.

References

- [1] Barbarino, S., Bilgen, O., Ajaj, R. M., Friswell, M. I., and Inman, D. J., "A review of morphing aircraft," *Journal of intelligent material systems and structures*, Vol. 22, No. 9, 2011, pp. 823–877.
- [2] Dhileep, K., Kumar, D., Ghosh, S., and Faruque Ali, S., "Numerical Study of Camber Morphing in NACA0012 Airfoil," *AIAA AVIATION 2020 FORUM*, 2020, p. 2781.
- [3] Namgoong, H., Crossley, W. A., and Lyrintzis, A. S., "Morphing airfoil design for minimum drag and actuation energy including aerodynamic work," *Journal of aircraft*, Vol. 49, No. 4, 2012, pp. 981–990.
- [4] Yokozeki, T., Sugiura, A., and Hirano, Y., "Development and wind tunnel test of variable camber morphing wing," *22nd AIAA/ASME/AHS adaptive structures conference*, 2014, p. 1261.
- [5] Munday, D., and Jacob, J., "Active control of separation on a wing with oscillating camber," *Journal of aircraft*, Vol. 39, No. 1, 2002, pp. 187–189.
- [6] Woods, B. K. S., and Friswell, M. I., "Preliminary investigation of a fishbone active camber concept," *Smart Materials, Adaptive Structures and Intelligent Systems*, Vol. 45103, American Society of Mechanical Engineers, 2012, pp. 555–563.
- [7] Diaconu, C. G., Weaver, P. M., and Mattioni, F., "Concepts for morphing airfoil sections using bi-stable laminated composite structures," *Thin-Walled Structures*, Vol. 46, No. 6, 2008, pp. 689–701.
- [8] Pontecorvo, M. E., Barbarino, S., Murray, G. J., and Gandhi, F. S., "Bistable arches for morphing applications," *Journal of intelligent material systems and structures*, Vol. 24, No. 3, 2013, pp. 274–286.
- [9] Saggere, L., and Kota, S., "Static shape control of smart structures using compliant mechanisms," *AIAA journal*, Vol. 37, No. 5, 1999, pp. 572–578.
- [10] Bartley-Cho, J. D., Wang, D. P., Martin, C. A., Kudva, J. N., and West, M. N., "Development of high-rate, adaptive trailing edge control surface for the smart wing phase 2 wind tunnel model," *Journal of Intelligent Material Systems and Structures*, Vol. 15, No. 4, 2004, pp. 279–291.
- [11] Sofla, A. Y., Elzey, D. M., and Wadley, H. N., "An antagonistic flexural unit cell for design of shape morphing structures," *ASME International Mechanical Engineering Congress and Exposition*, Vol. 47004, 2004, pp. 261–269.
- [12] Sofla, A., Elzey, D., and Wadley, H., "Cyclic degradation of antagonistic shape memory actuated structures," *Smart Materials and Structures*, Vol. 17, No. 2, 2008, p. 025014.

- [13] Sofla, A., Elzey, D., and Wadley, H., “Two-way antagonistic shape actuation based on the one-way shape memory effect,” *Journal of Intelligent Material Systems and Structures*, Vol. 19, No. 9, 2008, pp. 1017–1027.
- [14] Bhattacharyya, A., Conlan-Smith, C., and James, K. A., “Design of a bi-stable airfoil with tailored snap-through response using topology optimization,” *Computer-Aided Design*, Vol. 108, 2019, pp. 42–55.
- [15] Nordin, E., “Development of Body and Viscous Contribution to a Panel Program for Potential Flow Computation: Aero Dynamic Analysis and Preliminary Design Tool,” , 2006.
- [16] Morris, M., and Post, S., “Force Balance Design for Educational Wind Tunnels,” *American Society for Engineering Education*, American Society for Engineering Education, 2010.
- [17] Métivier, V., Dumas, G., and Poirel, D., “Aeroelastic dynamics of a NACA 0012 airfoil at transitional Reynolds numbers,” *39th AIAA Fluid Dynamics Conference*, 2009, p. 4034.
- [18] Sigmund, O., and Petersson, J., “Numerical instabilities in topology optimization: a survey on procedures dealing with checkerboards, mesh-dependencies and local minima,” *Structural optimization*, Vol. 16, No. 1, 1998, pp. 68–75.
- [19] Jog, C. S., and Haber, R. B., “Stability of finite element models for distributed-parameter optimization and topology design,” *Computer methods in applied mechanics and engineering*, Vol. 130, No. 3-4, 1996, pp. 203–226.
- [20] Bruns, T., Sigmund, O., and Tortorelli, D. A., “Numerical methods for the topology optimization of structures that exhibit snap-through,” *International Journal for Numerical Methods in Engineering*, Vol. 55, No. 10, 2002, pp. 1215–1237.
- [21] Kim, N.-H., *Introduction to nonlinear finite element analysis*, Springer Science & Business Media, 2014.
- [22] Belytschko, T., Liu, W. K., Moran, B., and Elkhodary, K., *Nonlinear finite elements for continua and structures*, John wiley & sons, 2013.
- [23] Basar, Y., and Weichert, D., *Nonlinear continuum mechanics of solids: fundamental mathematical and physical concepts*, Springer Science & Business Media, 2013.
- [24] Batoz, J.-L., and Dhatt, G., “Incremental displacement algorithms for nonlinear problems,” *International Journal for Numerical Methods in Engineering*, Vol. 14, No. 8, 1979, pp. 1262–1267.
- [25] Sigmund, O., “On the usefulness of non-gradient approaches in topology optimization,” *Structural and Multidisciplinary Optimization*, Vol. 43, No. 5, 2011, pp. 589–596.
- [26] Svanberg, K., “The method of moving asymptotes—a new method for structural optimization,” *International journal for numerical methods in engineering*, Vol. 24, No. 2, 1987, pp. 359–373.
- [27] Karush, W., “Minima of functions of several variables with inequalities as side conditions,” *Traces and Emergence of Nonlinear Programming*, Springer, 2014, pp. 217–245.
- [28] Kuhn, H. W., “Nonlinear programming: a historical view,” *Traces and Emergence of Nonlinear Programming*, Springer, 2014, pp. 393–414.
- [29] Thwaites, B., “Approximate calculation of the laminar boundary layer,” *The Aeronautical Quarterly*, Vol. 1, No. 3, 1949, pp. 245–280.
- [30] Blasius, H., “The boundary layers in fluids with little friction,” 1950.
- [31] Jacobs, E. N., and Abbott, I. H., *Airfoil section data obtained in the NACA variable-density tunnel as affected by support interference and other corrections*, 669, US Government Printing Office, 1939.
- [32] Ge, D. C. Q. H., Q., and M.L., D., “Active origami by 4D printing,” *Smart Materials and Structures*, Vol. 23, No. 9, 2014, p. 094007.